A review on voids of 3D printed parts by fused filament fabrication

8 authors, including:

Yubo Tao
Qilu University of Technology
42 PUBLICATIONS   **343** CITATIONS

SEE PROFILE

Fangong Kong
Qilu University of Technology
218 PUBLICATIONS   **2,270** CITATIONS

SEE PROFILE

Zelong Li
3 PUBLICATIONS   **163** CITATIONS

SEE PROFILE

Jingfa Zhang
Université du Québec en Abitibi-Témiscamingue
16 PUBLICATIONS   **120** CITATIONS

SEE PROFILE

Some of the authors of this publication are also working on these related projects:

Project   Electrochemistry of Dealloyed Nanoporous Materials (Qilu University of Technology) View project

Project   Electrocatalysis (HER, OER, ORR, CRR, NRR, ECH, ECO, etc.) View project

Review Article

A review on voids of 3D printed parts by fused filament fabrication

Yubo Tao [a], Fangong Kong [a], Zelong Li [b], Jingfa Zhang [a], Xin Zhao [a], Qing Yin [a], Dan Xing [a], Peng Li [a,*]

[a] State Key Laboratory of Biobased Material and Green Papermaking, Qilu University of Technology (Shandong Academy of Sciences), Jinan, China
[b] Department of Computer Science, The University of British Columbia, Vancouver, Canada

ARTICLE INFO

ABSTRACT

Fused filament fabrication (FFF), also known as fused deposition modeling (FDM™), is considered one of the most promising additive manufacturing (AM) methods for its versatility, reliability and affordability. First adopted by industries for professional uses such as rapid prototyping, then by the general public in recent years, FFF has gathered itself considerable attention. Nevertheless, despite key advancements in printer technologies and filament materials, the fabrication of robust, performing and functional parts for high-demanding practical applications remains a significant challenge. Due to intrinsic deficiencies, such as the presence of voids and weak layer-to-layer adhesion, FFF-printed parts are plagued by weak and anisotropic mechanical properties in contrast to their conventionally manufactured counterparts. With the increasing demand for designable porous structures in the fields of biomedicine, 4D printing and lightweight cellular composites, understanding the challenges presented by void presence has become more relevant than ever. As existing literature has reviewed the significance of interlayer bonding, this review focuses on documenting recent insights on the formation of voids by its categorization, research method and mechanism. The primary objective is to provide a comprehensive understanding of the two current primary methods of void research—quantitative analysis and imaging. Detailed discussions on the effects of feedstock and printing parameters on void formation are also presented. Lastly, this review discusses gaps in the current research and outlines unaddressed challenges regarding void formation and its relation with the mechanical performance of FFF parts.

Nomenclature

AM	Additive manufacturing
ME	Material extrusion
BJ	Binder jetting
MJ	Material jetting
SL	Sheet lamination
PBF	Powder bed fusion
VP	Vat photo polymerization
DED	Directed energy deposition
FFF	Fused filament fabrication
FDM™	Fused deposition modeling
ABS	Acrylonitrile butadiene styrene
ASA	Acrylonitrile styrene acrylate
IM	Injection molding
PA	Polyamide
PLA	Polylactic acid
PEG	Poly(ethylene glycol)
PETG	Polyethylene terephthalate glycol
TPU	Thermoplastic polyurethane
PVA	Polyvinyl alcohol
PET	Polyethylene terephthalate
POM	Polyoxymethylene
PEEK	Polyetherether-ketone
PVDF	Polyvinylidene fluoride
PEKK	Polyetherketoneketone
PPS	Polyphenylene sulfide
SDCNF	Spray-dried cellulose nanofibrils
PPco	Polypropylene block copolymer
HH	Industrial hemp hurd
OM	Optical microscope
SEM	Scanning electron microscopy
μCT	Micro computed tomography
CNF	Cellulose nanofiber
CF	Carbon fiber
LMW	Low molecular weight
DoE	Design of experiments
OFAT	One factor at a time
ANN	Artificial neural network
ML	Machine learning

1. Introduction

According to the ISO/ASTM 52900-15 standard, additive manufacturing (AM), commonly known as 3D printing, is the 'process of joining materials to make parts from 3D model data, usually layer upon layer' [1,2]. At the time of writing, commercially available AM technologies are classified into seven categories—material extrusion (ME), binder jetting (BJ), material jetting (MJ), sheet lamination (SL), vat photo-polymerization (VP), powder bed fusion (PBF) and directed energy deposition (DED) [3,4]. In particular, ME has become the most popular and widely available AM category to date for its cost-effectiveness and easy accessibility [5,6]. As the name implies, ME builds sliced 3D models layer-by-layer with viscous material (in paste or semi-liquid form) extruded through a nozzle or orifice [7]. Applications of ME include

direct ink writing (DIW) [8,9], 3D concrete printing [10] and fused filament fabrication (FFF) [11]—also known as fused deposition modeling (FDM™) [12,13].

FFF is arguably the most widespread ME-based AM technique [5,6]. By virtue of its comparative advantages—open-source instruments [4], cost effective feedstock materials [15], versatile build volumes and scales [16,17] and the ability of co-printing multiple compositions for functionally graded parts [7,18]—FFF has become a critical industrial tool for design and manufacturing in fields [19], such as aerospace [20], biomedical sciences [21,22], electronic sensors [23] and automobile manufacturing [24].

Moreover, FFF is compatible with a broad selection of materials [15], most commonly including amorphous thermoplastics, such as acrylonitrile butadiene styrene (ABS) [25], semicrystalline polymers, such as polylactic acid (PLA) [26,27] and their composites [16,28]. Filament materials such as PLA, thermoplastic polyurethane (TPU), polyvinyl alcohol (PVA) and polyethylene terephthalate (PET) are popular in the consumer market [29,30]. On the other hand, engineering plastics, such as polyamides (PA), ABS, TPU, PET and polyoxymethylene (POM), are oriented to professional and industrial fields [29]. In addition, the commercialization of high-performance filament materials, such as polyetherether-ketone (PEEK), polyvinylidene fluoride (PVDF), poly-etherketoneketone (PEKK) and polyphenylene sulfide (PPS), has furthered the adoption of FFF technologies in industry [29].

Despite the promising future enabled by its wide spectrum of compatible polymer and composite materials, certain shortcomings of FFF have constrained its industrial utilization. Notably, FFF prints are generally less mechanically capable than their conventionally manufactured, polymer-processed counterparts, such as via injection molding (IM) [31–33]. These deficiencies are primarily a result of the nature of the FFF mechanism. To better understand their origins, the working principle of FFF is presented in Fig. 1. Material filament is first driven into the print head by a pinch wheel. Passing through a liquefier, the feedstock is heated to a viscous melt and pushed out of the print nozzle by the
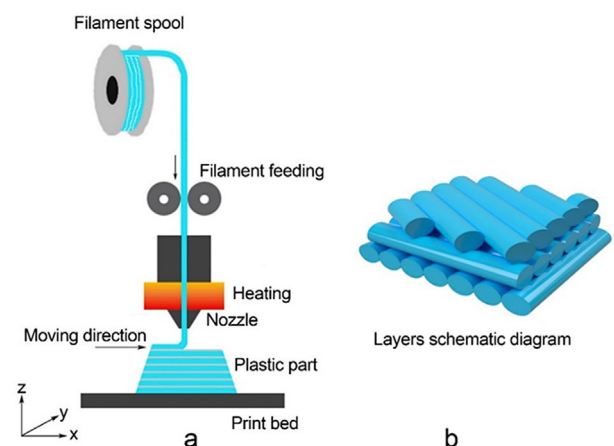

Fig. 1 – **Illustration of an FFF: (a) FFF printing mechanics; (b) layers schematic diagram [14].**
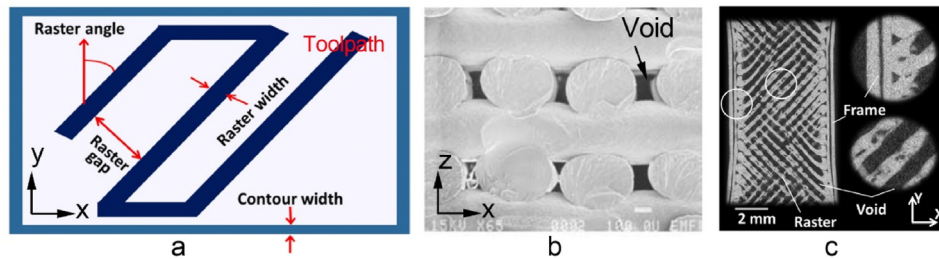
Fig. 2 — Raster gap voids: (a) diagram of an FFF layer [54]; (b) XZ cross-sectional view of a part with orthogonal rasters [55]; (c) YZ cross-sectional view of a printed nylon microstructure [56].

incoming still-solid filament. FFF printers configured with a Z-direction moving print bed are coupled with a gantry that moves the print head in the X—Y plane. For printers with a fixed print bed, the gantry covers movement in all directions. Routes followed by the print nozzle are named toolpaths. Following these pre-computed toolpaths, the melts resolidify after leaving the nozzle to form each layer of the print [34,35]. Notably, FFF printers are capable of constructing 3D components with a dimensional accuracy in the order of 100 μm [4,5,15,36].

Uncontrollable pressures after the melt leaves the moving print head, coupled with rapidly decreasing temperatures, means that sufficient bonding between material strands is not guaranteed during the deposition process [37]. Furthermore, the viscous melts low flowability and diffusion further weaken raster-to-raster adhesion [38]. Studies on weak interlayer bonding in FFF has been reviewed by Gao et al. [4]. In addition to interlayer bonding, the effects of porous structures or voids on the mechanical performance of FFF parts are also noteworthy. In general, part performance is reduced by stress concentrations formed at pores or voids [39,40]. During the FFF process, melts experience shear and elongation, resulted by nozzle movement, and melt flow is stretched into elliptical cylinders, as shown in Fig. 1b. Voids (pores) formed in-between deposited rasters [16,32,41—44] are detrimental to the stiffness, strength and density of printed parts [45—48].

Nevertheless, designable and regulated porous structures are desirable for certain cutting-edge applications, such as biomedicine [22,49,50], 4D printing [51,52] and lightweight cellular composites [53]. In order to control or minimize the effects of voids on FFF part properties, there is great utility in identifying the factors that are correlated with the formation of voids. At the time of writing, there are no known published reviews on FFF void formation and characterization.

In hope of contributing to a more comprehensive understanding of FFF voids, this paper aims to summarize, present and analyze studies published in the past two decades. The review is structured as follows. Section 1 provides a brief overview of categorization of voids. Section 2 introduces the current experimental methodologies, such as image analyses and porosity measurements. Section 3 discusses the numerical simulation of void formation. Section 4 covers effects of processing parameters on voids. Lastly, section 5 summarizes the conclusions of the study.

2. Categorization of voids

The desirability of voids in FFF parts is dependent on the designated application. Desirable voids are 3D structural elements designed to reduce weight and/or improve functionality. Whereas, voids are undesirable for applications requiring optimal mechanical performance. Overall, FFF voids could be classified into five categories by their mechanism of formation: (1) raster gap voids, (2) partial neck growth voids, (3) sub-perimeter voids, (4) intra-bead voids, (5) infill voids.
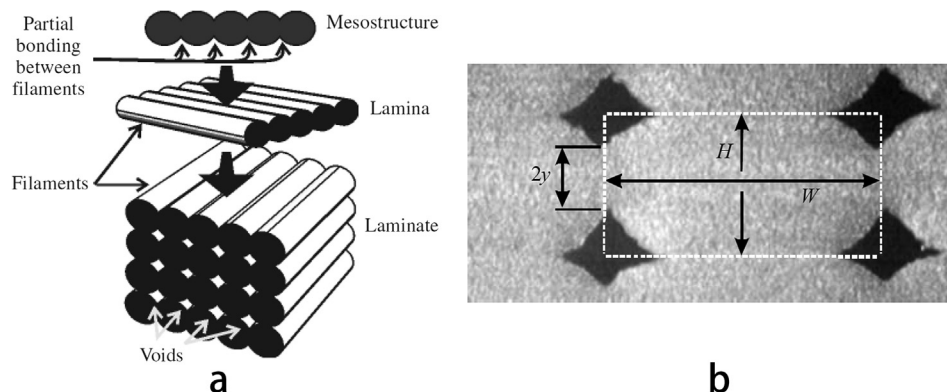
Fig. 3 — Partial neck growth voids: (a) Break down of the FFF part structure: laminae stacked in a layer-upon-layer fashion create the laminate; rasters ("filaments" in the diagram) on the same plane bond to form a lamina; rasters experience partial bonding in the part mesostructure [42]; (b) Cross-sectional view of an FFF laminate, where W is the raster width, H is the raster height and 2y is the neck growth between adjacent rasters [63].
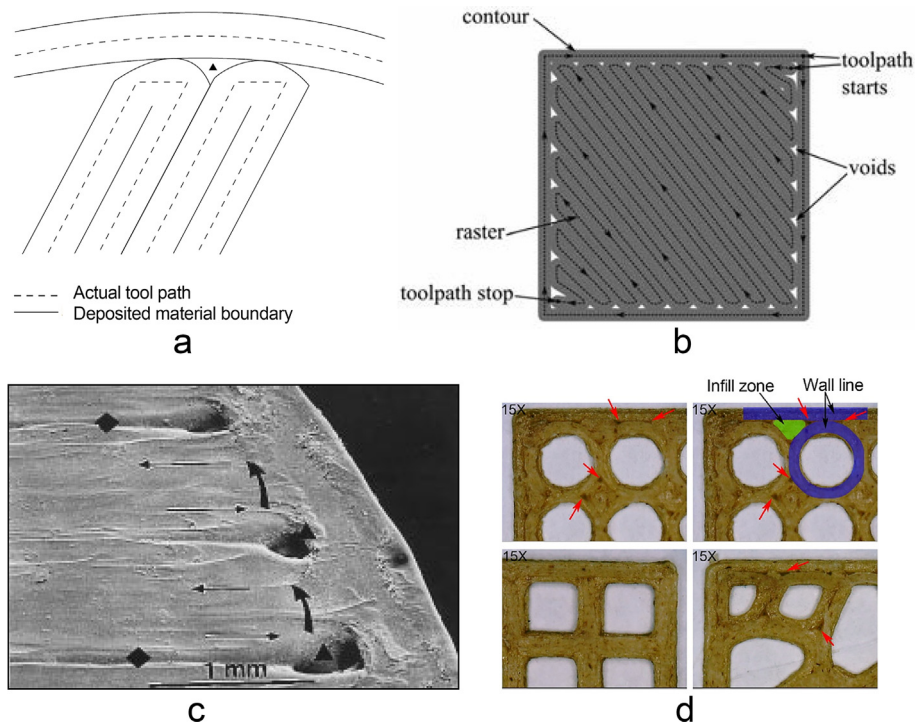
Fig. 4 – Sub-perimeter voids: (a) Sub-perimeter void formation diagram. The region marked by ▲ is a sub-perimeter void that formed in-between the perimeter and the rasters [68]; (b) Diagram for a generic rectangular FFF layer [34]; (c) SEM micrograph of the top surface of an FFF part with sub-perimeter voids (s) [68]; (d) Specimen cross sections. Red arrows point at sub-perimeter voids [59].

2.1. Raster gap voids

Fig. 2a is an abstract representation of the cross-sectional layer of a typical rectangular FFF part. The perimeter of a layer is defined by its contour [57] (also referred to as shell [58], wall [59] or frame [56]). This established area is filled in with rasters [54] (also known as roads [55], beads [12]), strands [11] or filaments [42]) in accordance with the designated infill pattern, as dictated by the toolpaths computed in the slicing software. Raster gaps (also named air gaps [60] or road width

[61]) are the separation between adjoining rasters. This parameter is negative for overlapping rasters [62]. In general, an infill pattern of sparser raster spacings naturally results in larger raster gaps, which in turn creates larger internal voids. These voids formed by gaps between the rasters are distinctively visible in Fig. 2b and c. Undesirable raster gap voids degrade the printed parts mechanical performance. However, when used constructively, printing with larger raster gaps could reduce the overall built time and feedstock usage [34]. Thus, raster gaps and their related parameters are influential
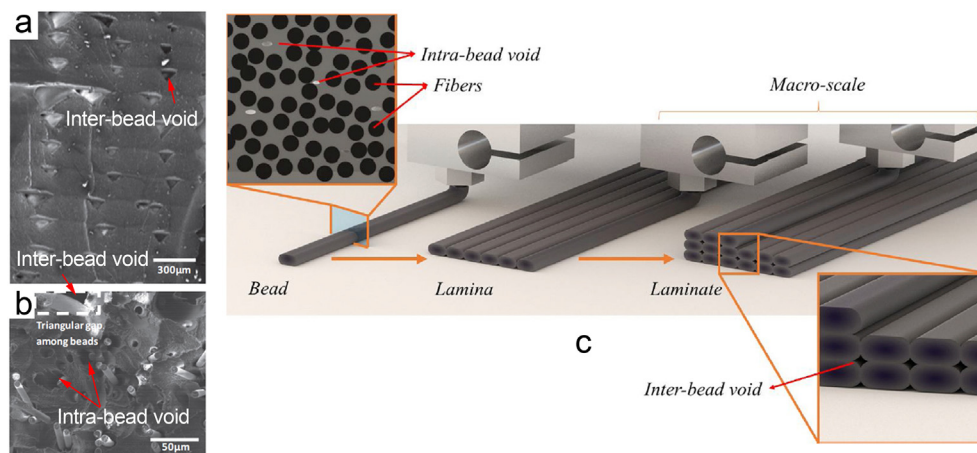

Fig. 5 – Intra-bead void: (a) neat-ABS FFF part [69]; (b) 10 wt% carbon fiber (CF)-loading part [69]; (c) Voids in a multiscale structure FFF print of fiber-reinforced composite materials [39].
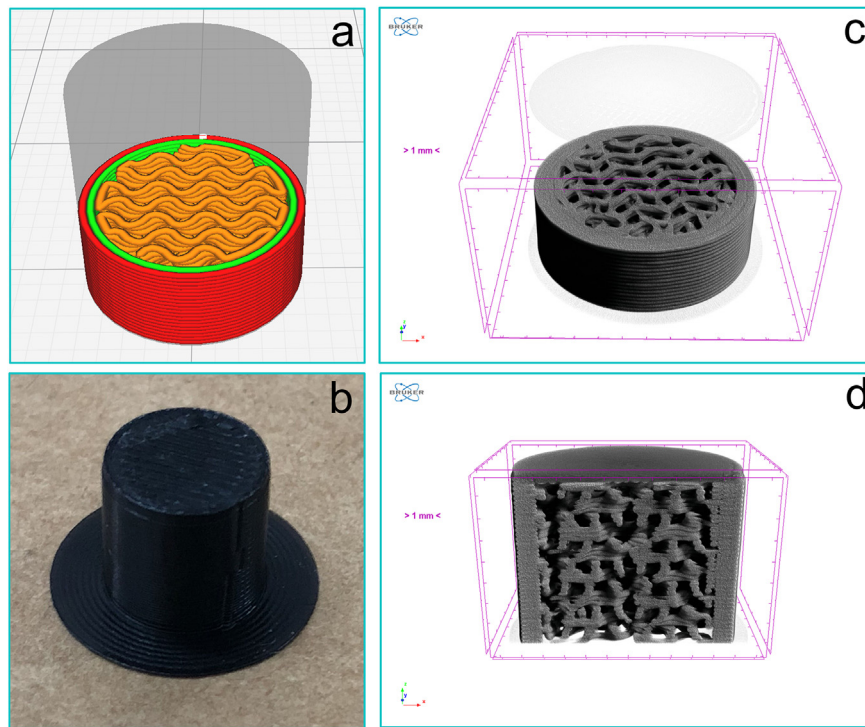
Fig. 6 – µCT imaging of an FFF part with gyroid infill: (a) model slicing; (b) printed part; (c) XY cross-section of part; (d) XZ cross-section of part.

factors in FFF part production. More specifically, raster gaps could be adjusted to control and design part performance.

2.2.   *Partial neck growth voids*

As shown in Fig. 3a, internal voids could form as a result of the incomplete neck growth between adjoining intra-layer and inter-layer [61] rasters (named 'filaments' in the diagram). As a product of the mechanism of viscous sintering, void formation in FFF parts is dependent on the neck growth between neighboring rasters. In the ideal circumstance of 100% coalescence between two adjacent rasters, this type void formation would be physically impossible. However, realistic conditions during the FFF process are incapable of sustaining neck growth beyond a brief few seconds after material deposition [64]. In other words, the rasters would solidify before completing coalescence [65,66]. Partial neck growth voids formed in-between rasters and layers (or laminae) are impossible to eliminate entirely due to certain inherent, inevitable characteristics of the FFF process, such as incomplete filling and inconsistent material flow [67]. Hence, partial neck growth voids are major contributors to void presence in FFF prints.

2.3.   *Sub-perimeter voids*

As shown in Fig. 4, sub-perimeter voids are formed in-between turning rasters along the perimeter of an FFF layer due to physical limitations. Standard print paths, such as
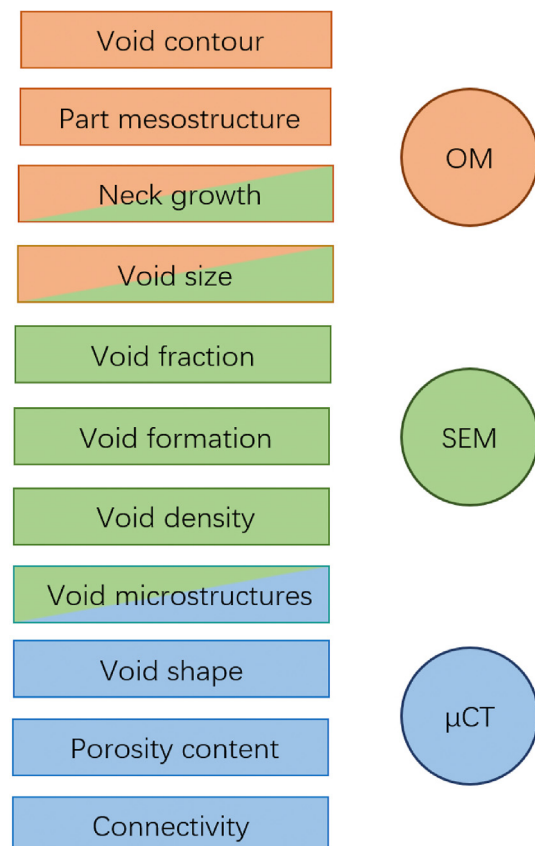

Fig. 7 – Imaging techniques for void study in existing literature.

Table 1 – Imaging techniques.

Methods	Study objectives
OM	The neck growth variation between adjacent filaments of printed ABS P400 parts for various processing conditions [63].
	The mesostructures and normalized contact lengths of printed ABS parts [71].
	The influence of different parameters on voids and gaps in cross-sections of the PLA specimens [38].
	The contour of material strands and voids in printed PLA parts [11].
SEM	The fractured surfaces of printed PLA parts and injection molded components. The effect of plate temperature and layer height on void size [26].
	The effects of various printing parameters (printing temperature, printing speed, etc.) on the microstructure of printed PEEK parts [72].
	The effect of chopped Hexcel AS4 carbon fiber loading on void formation in printed ABS parts [69].
	The effect of infill patterns on void structures in PLA parts [73,74].
	The effect of extrusion temperature and layer height on the number of cells and cell sizes in printed PP parts [75].
	The freeze fracture surfaces and void sizes of printed PA1012 parts with a raster angle of 0° at various nozzle temperatures [76].
	The microstructure and void sizes of printed ABS parts at various nozzle and print bed temperatures [77].
	The effects of the addition of PEG with various molecular weights in PLA on neck growth in printed parts [78].
	The effects of low molecular weight PLA (8.5 k, 50 k and 100 k at 10 mol%) on the spacing between filaments in printed parts [79].
μCT	The microstructures of printed parts, analyzed the porosity content profiles of 3D stacks in all spatial directions and revealed the porous structures in parts printed with nylon [56], wood-PLA/PHA [80], hemp-PLA [81], PETG [82] and acrylonitrile styrene acrylate (ASA) [83].
	Void shapes in printed ABS-M30 parts along the XYZ axes [84].
	Porous structures, three phases: pore, Nylon-12 and short carbon fiber (SCF) in printed composite part [85].
	Quantify structural attributes such as porosity content and connectivity. Analyzed image data with finite element models to study effects of process-induced defects on the part mechanical performance [86].
	Comparing of void variation inside and outside nozzle, as well as the prints [87].
	Tomogram images of void shape, orientation and fraction variation along the printing direction [88].

those in Fig. 4a and b, fill in a print layer area by reversing their direction at the perimeter. However, more complete raster fillings would require sharper U-turns, which are accompanied by higher centripetal acceleration. In order to reduce the adverse effects of centrifugal forces on the stepping motors without significant scarifies in build time, FFF printers must compensate by replacing all sharp corners with approximated curves. Consequently, as a result of these softer curves, the insufficient material flow during deposition leaves behind gaps and voids in FFF layers, as seen in Fig. 4c [68]. Moreover, sub-perimeter voids are visually identifiable, such as in Fig. 4d. Despite having an infill density of 100% (as specified in the slicing software), voids formed between the blue wall lines and the green infill zones [59].

2.4. Intra-bead voids

Intra-bead voids are specific to FFF parts of composite materials. Fig. 5a and b illustrate the effects of fiber loading on intra-bead void formation. Partial neck growth voids are the only void type present in the neat-ABS sample shown in Fig. 5a. As expected, these voids are fairly consistent in shape, orientation and distribution. In comparison, along with the triangular partial neck growth voids, additional porous

structures of smaller scales are identifiable in the carbon fiber/ABS composites in Fig. 5b [69]. As depicted in Fig. 5c, intra-bead voids in the material filament persist in the multiscale FFF structure after deposition [39]. Notably, substantial porosity up to an approximated 20% has been found in FFF prints using wood fiber reinforced biocomposites [52].

2.5. Infill voids

Unlike the previously mentioned categories, infill voids are controllable and desirable void formations. FFF oriented slicing software generally incorporate user-definable infill densities and a variety of user-selectable infill patterns, such as grid, lines, triangles, concentric, zig-zag, cross and gyroid. For less mechanically, functionally or visually demanding applications, lower infill densities are ideal for reducing material usage and overall build time. Whereas higher infill densities would result in more solid and generally stronger prints, at the cost of materials and a lengthier build time. The infill patterns of choice have distinctive beneficial effects on reducing the weight and increasing the strength of FFF parts. For example, the gyroid infill, as shown in Fig. 6, increases a part strength in all directions (XYZ) for the lowest possible weight [70].

3. Study methods for voids

3.1. Imaging techniques

The porosity of FFF parts could be obtained by comparing its density to the density of identical injection molded specimens [32] or the density of compressed filaments [52]. In addition to density measurement, imagining techniques, including OM, SEM and µCT, are commonly used in existing literature to study FFF voids. The diagram presented in Fig. 7 breaks down the information regarding voids obtainable from each imaging technique. OM is a commonly used technique for studying the mesostructures of printed parts, whereas SEM is often used to analyze microstructures. OM and SEM are both capable of capturing 2D imaging data along the X/Y/Z planes (axes). Moreover, images orthogonal to FFF layers are valuable data for the analysis of raster gap voids, partial neck growth voids and intra-bead voids. Similarly, images parallel to FFF layers could be used to study sub-perimeter voids. In addition to the imaging capabilities of OM and SEM, µCT could be used to reconstruct 3D models of scanned specimens in great detail. Therefore, µCT is a valuable tool for observing and investigating effects of FFF voids in three dimensions. The objectives of each study utilizing the corresponding imaging technique are summarized in Table 1.

3.2. Quantitative analysis

While visual comparisons of void shapes and sizes that could be made by directly observing images, quantitative analysis is necessary for obtaining accurate measurements. Existing literature has found that certain characteristic parameters of FFF voids could be derived from imaging data and density measurements. Formulae for each parameter found in past studies are listed in Table 2.

3.3. Modeling

Partial neck growth voids are primary contributors to void presence in FFF parts. Therefore, neck growth models are focused on in existing literature. An early model for the time evolution (read chronologically from left to right) of a pair of coalescing Newtonian fluid droplets based on viscous dissipation and surface tension is shown in Fig. 8a [89]. The spherical droplets of radius a_0 are assumed to be spatially identical and centered at points A and B, respectively. The model operates in an idealized scenario where all external forces, such as gravity, are ignored. Let $t = 0$ when the spheres only point of contact is at location O. After some arbitrary amount of time t, the spheres centers undergo translation towards point O and coalesce into joint spheres of radius $a(t)$, where $\theta(t)$ is the intersection angle between the two spheres and $x(t)$ is the radial width of neck growth. Eventually, these droplets will coalesce into one sphere of radius a_f, such that A = B = O. A quantitative relationship between $a(t)$ and $\theta(t)$ based on the conservation of mass for a fluid of constant density could be established as follows:

$$a(t) = a_0 \left(\frac{4}{(1 + \cos(\theta(t)))^2 (2 - \cos(\theta(t)))} \right)^{\frac{1}{3}} \tag{1}$$

$$\frac{d\theta(t)}{dt} = \frac{\Gamma}{a_0 \eta} \frac{2^{-5/3} \cos(\theta(t))\sin(\theta(t))[2 - \cos(\theta(t))]^{1/3}}{[1 - \cos(\theta(t))][1 + \cos(\theta(t))]^{1/3}} \tag{2}$$

$$\frac{x(t)}{a(t)} = \sin(\theta(t)) \tag{3}$$

$$\frac{x(t)}{a_0} = \sin(\theta(t)) \left(\frac{4}{[1 + \cos(\theta(t))]^2 [2 - \cos(\theta(t))]} \right)^{1/3} \tag{4}$$

where Γ is the coefficient of surface tension, η is the viscosity [89]. Existing literature have used this model to describe neck growth during the FFF process [42,63].

Nevertheless, there exist models specific to represent raster neck growth. For instance, as shown in Fig. 8b [61], the following model for neck growth evolution was established by considering neighboring cylindrical filaments:

$$\frac{d\theta}{dt} = \frac{\Gamma}{3\sqrt{\pi}r_0 \eta} \left[\frac{[(\pi - \theta)\cos\theta + \sin\theta][\pi - \theta + \sin\theta\cos\theta]^{1/2}}{(\pi - \theta)^2 \sin^2\theta} \right] \tag{5}$$

where r_0 is the initial radius of the cylindrical filaments [61].

Furthermore, Bhalodi et al. [66] applied the RK4 method to Eq. (2) and Eq. (5) to obtain the following differential equations that relate neck growth with temperature:

$$\frac{d\theta}{dT} = \frac{\Gamma}{mva_0 \eta(T - T_\infty)} \left[\frac{2^{-5/3} \cos(\theta)\sin(\theta)[2 - \cos(\theta)]^{1/3}}{[1 - \cos(\theta)][1 + \cos(\theta)]^{1/3}} \right] \tag{6}$$

$$\frac{d\theta}{dT} = \frac{\Gamma}{3\sqrt{\pi}mvr_0 \eta(T - T_\infty)} \left[\frac{[(\pi - \theta)\cos\theta + \sin\theta][\pi - \theta + \sin\theta\cos\theta]^{1/2}}{(\pi - \theta)^2 \sin^2\theta} \right] \tag{7}$$

where m is mass of the filament, v is velocity of extrusion nozzle and T_∞ is envelope temperature or build plate/print bed temperature [66].

Fig. 8c and d [90] present a model for the time evolution (read chronologically from top to bottom) of coalescing rasters with stadium-shaped cross-sections of consistent height H_0. Its cross-sectional geometry aims to better resemble rasters during FFF sintering than past circular/cylindrical models. Let $t = 0$ when the two stadiums only point of contact is location O, such that each stadium is composed of two semicircles of radius $H_0/2$ and a rectangle with an initial width w_0 and height H_0. After some arbitrary amount of time t, the contacting semicircles translate toward point O and coalesce into one joint body, where $\theta(t)$ is the intersection angle and $y(t)$ is the radial width of neck growth. The width of the rectangular section of the stadiums $w(t)$ changes with coalescence. A quantitative relationship between $w(t)$ and $\theta(t)$ based on the conservation of mass for two coalescing fibers of constant density could be established as follows:

$$w(t) = w_0 + \frac{H_0 \theta(t)}{4} - \frac{H_0 \sin(2\theta(t))}{8} \tag{8}$$

Table 2 – Quantitative analysis.

Data source	Void parameters	Methods
SEM/OM	Void size	The volume-averaged diameter of all of the cells (voids) in the micrograph, D_v, $$D_v = \left[\frac{\sum_{i=1}^{n} d_i^3}{n}\right]^{\frac{1}{3}}$$ where n is the number of cells and d_i^3 is the perimeter-equivalent diameter of each counted cell [75].
	Void density	N_f is the number of cells per unit volume of foam and was originally calculated by $N_f = \frac{n}{A}$ where n is the number of cells in a micrograph of area A [75].
	Void fraction	Void fraction is determined as: $$\varphi = \left(1 - \frac{1}{\varnothing}\right) \times 100\%$$ where $\varnothing$ is the expansion ratio [75]. Void fraction is determined as: $$Void\ fraction = \frac{pixels\ of\ void\ space}{total\ pixels\ of\ image}\ [79].$$
μCT	Porosity content	$f(\%)$ is the porosity volume percentage $$f(\%) = 100 \times \left(\sum_{i=1}^{n \times m \times l} \delta_i^1(g_i) \Big/ \sum_{i=1}^{n \times m \times l} \delta_j^2(g_j)\right)$$ δ_i is the Kronecker's function, which depends on the grey level g_i associated to voxel i; n, m and l are the dimensions of the X-ray image in X, Y and Z directions, respectively [86].
	Pore connectivity	$$\gamma(\%) = 100 \times Max_{i=1}^{N}(V_p(i)) \Big/ \sum_{i=1}^{N} V_p(i)$$ where γ is the pore connectivity percentage, $V_p(i)$ is the volume associated to the labelled pore i, N is the total pore number [86].
Specimen density measurement	Porosity	$$Porosity(\%) = \frac{(\rho_{injection} - \rho_{FDM})}{\rho_{injection}} \times 100$$ where $\rho_{injection}$ is the average density of injection molded specimens and ρ_{FDM} is the average density of FDM specimens [32]. $$Porosity(\%) = \frac{(\rho_{compressed\ filament} - \rho_{sample})}{\rho_{compressed\ filamen}} \times 100$$ Porosity is obtained by comparing the density of compressed filaments and printed samples [52].

$$\frac{d\theta(t)}{dt} = \frac{\Gamma(T_r(x,t))H_0}{4\eta(T_r(x,t))} \frac{2\cos(\theta(t))^2}{\left(\pi\left(\frac{H_0}{2}\right)^2 + H_0 w_0\right)\left(\frac{-\frac{H_0}{2}\sin(\theta(t))+\frac{H_0}{8}-\frac{H_0}{8}\cos(2\theta(t))}{\frac{H_0}{2}+\frac{w_0}{2}}\right)^2}$$ (9)

$$y(t) = \frac{H_0}{2}\sin(\theta(t))$$ (10)

The distance between the center of the semicircles and point O is:

$$\delta = \frac{H_0}{2}\cos(\theta(t))$$ (11)

Lastly, void density can thus be calculated as follows: [90].

$$\rho_{voids} = \frac{Total\ area\ of\ voids}{Total\ cross-section\ area} = \frac{H_0^2\cos(\theta(t)) - \left[\pi\left(\frac{H_0}{2}\right)^2(2\theta(t) - \sin(2\theta(t)))\right]}{H_0 w(t) + H_0^2\cos(\theta(t))}$$ (12)

where $T_r(x, t)$ is the raster temperature at time t.

The radial width of neck growth $y(t)$ could be computed from the intersection angle $\theta(t)$ and the raster height H_0 with the following relation:

Notably, void density in Eq. (12) is different from the definition given by Wang et al. [75].

Evidently, neck growth models employed in current research has grown increasing realistic in emulating the
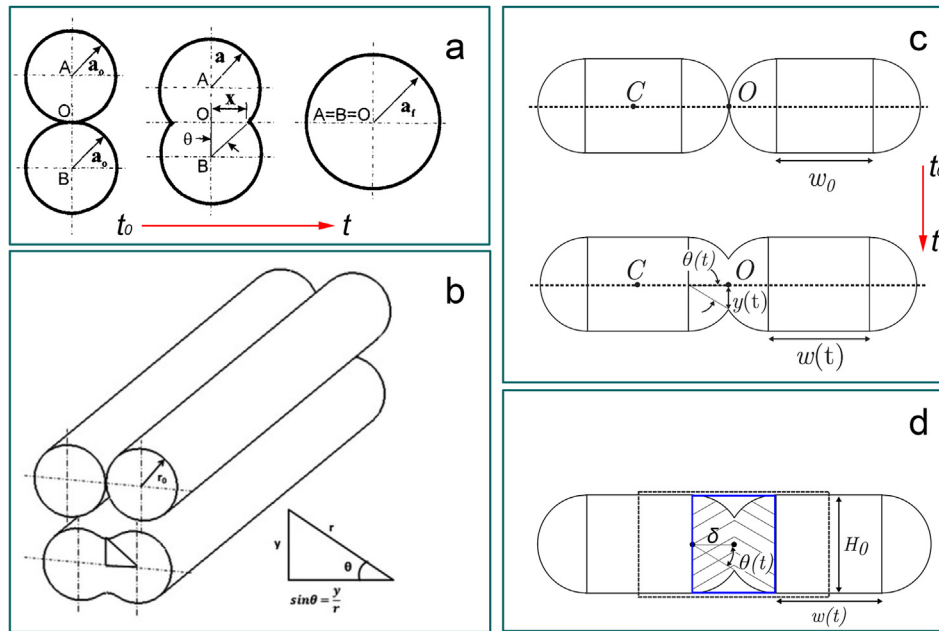
Fig. 8 – Neck growth models: (a) Diagram of the coalescence of identical particles under the action of surface tension [89]; (b) Material bonding process during the FFF [61]; (c) Bonding between two adjacent rasters [90]; (d) Post-bonding geometry of adjacent rasters [90].

geometry and characteristics of deposited melts. Coupled with the information/data from imaging techniques such as OM, SEM and μCT, minute features in the microstructure of FFF parts are now observable and increasingly controllable.

4. Effects of feedstock and processing parameters on voids

Feedstock material and processing parameters, such as nozzle temperature, print bed temperature, printing speed and layer height, have distinguishable effects on void formation in FFF parts. In particular, the influences of feedstock and processing parameters on FFF voids as investigated by existing literature are summarized in Table 3.

4.1. Effects of feedstock on voids

4.1.1. Fillers
Organic or inorganic fillers are commonly incorporated into polymer matrices to modify and enhance material properties and/or prepare environmental benign composites. Nonetheless, the addition of fillers could affect a material rheology, thermal properties and crystallization kinetics [29,91]. Viscosity, flowability and molecular mobility are all factors that influence void formation. More voids have been found to exist in the prints using polymer-based composite feedstocks [32,92−94]. Under consistent printing parameters, the welding process of deposited strands is determined by the composites flowability, macromolecular chain rearrangement and molecular chains interface diffusion [92,93,95]. The nucleation effects of fillers, such as CF, CNF and waste paper powder, have been found to affect the polymer crystallization process,

increase crystallinity and promote the formation of small crystals [6,29]. The presence of fillers and an increased quantity of imperfect crystalline structures in the composite materials may hinder the mobility of polymer chains and decrease interface diffusion. Consequently, a worsened welding process results in larger voids and higher porosity [92]. Apart from the larger inter-layer voids caused by fillers, Yang et al. [87] observed intra-bead voids in CF-nylon extrudates close to the print nozzle formed as a result of the pressure difference inside and outside of the nozzle. Notably, these intra-bead voids are reduced as temperatures decrease after deposition. However, some voids persist as the faster cooling rate of outer raster surface prevents the inner voids from completing shrinkage. Therefore, the effectiveness of decreasing intra-bead voids in FFF parts of porous materials through adjusting the 3D printing process itself is limited [88].

4.1.2. Plasticizers
Plasticizer is often used in polymer processing to modify flowability. In FFF, the addition of plasticizer in filament materials is beneficial for reducing voids in printed parts [78]. Using PEG as a plasticizer of PLA, Gao et al. observed enhanced mechanical performance in prints and smaller void size, as shown in SEM images (Fig. 9) [78]. Evidently, PEG is capable of facilitating the mobility of PLA chains and improving interface molecular diffusion and entanglements. Moreover, Ko et al. found that the lower viscosity brought about by TPP reduced void size and enhanced interdiffusion in PC-ABS parts with little sacrifice in mechanical performance [97]. Incorporation of low molecular weight (LMW) polymers is another route for improving raster-to-raster contact. For instance, Levenhagen et al. [79] mixed 8.5 k, 50 k and 100 k PLA into 220 k PLA. Their results demonstrated that LMW 50 k components improved

Table 3 – Effects of feedstock and processing parameters on void.

| Variables	Void size	Void density	Void fraction	Porosity	Void connectivity	Void shape
Fillers		The addition of filler (HH [32], SDCNF, CNF and CF [92,93]) increased the number of voids in printed parts [94].	Void fraction of CF-nylon filament changes with the printing process [87]. 3D printing parameters have limited effects on void fraction for CF-PEEK parts with a large quantity of voids [88].	The porosity content of nylon [56] was higher than wood-PLA/PHA [80], hemp-PLA [81], ASA [83] and PETG [82] under similar processing conditions.		
Plasticizers	The addition of PEGs in PLA [78] and TPP in PC-ABS [97] decreased the size of inter-filament voids.		Compared to 100 k low molecular weight PLA, the use of 8.5 k and 50 k PLA endowed void space fusion, but mechanical properties were degraded by the addition of 8.5 k PLA [79].		With the introduction of LMW additives, most voids were eliminated [98].	
Printing speed	Faster printing speed resulted in larger voids [71]	Lower printing speeds resulted in fewer voids [72].				
Plate/bed temperature	Higher print bed temperatures resulted smaller voids [26,77].					
Layer height	Thinner layer height results in smaller voids [26,77].	Thinner layer heights, or more layers, resulted in a larger void count [75].	Thicker layer heights resulted in larger void fractions [75].			
Raster width		Increased raster width results in fewer voids for a given area [77,101]				
Nozzle temperature/ printing temperature	Increase nozzle temperatures resulted in smaller partial neck growth voids [75–77].	Higher extrusion temperatures resulted in fewer voids [72,75,104].	Higher extrusion temperatures resulted in smaller void fractions [75].	Porosity content of nylon parts printed at 250 °C was higher than parts printed at 255 °C [56].	99% of the voids (porous structures) were connected [56].	
Position on the Z axis	Voids grew in size for layers further away from the build plate [63,75].					
Infill-patterns and density		Triangular infill resulted in fewer voids and effective raster bonding [73].	Increasing infill density can reduce void fraction [74].			
Build direction	Void growth was in the Z-, YZ- and Y-directions for samples in the edge, flat and upright orientations, respectively [84].			No obvious variations [84].		No obvious variations [84].
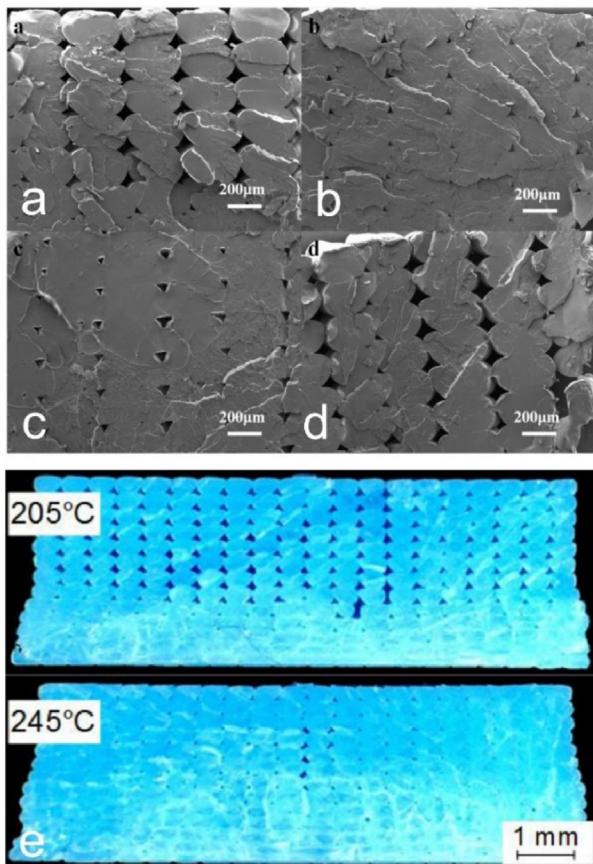
Fig. 9 – Effects of plasticizer (PEG with different molecular weight) and nozzle temperature on void size: (a) pure PLA; (b) PLA-PEG 4000; (c) PLA-PEG 8000; (d) PLA-PEG 20000 [78]; (e) void size decreases with the increase of nozzle temperature [96].

interlayer contact and reduced void fraction. Although 8.5 k PLA nearly eliminated void presence, the mechanical strength of the FFF specimens were severely degraded due to the lack of sufficient long polymer chain entanglements along the interface of adjacent strands. Increasing molecular weight to 100 k constrained interface diffusion and resulted in a larger void fraction. In addition, Levenhagen et al. found that, although linear LMW, 3-star additives and 4-star additives are all effective for reducing voids, parts with 3-star additives exhibited superior mechanical performance [98]. In summary, although LMW polymers are viable candidates for effectively reducing FFF voids, their detrimental effects on mechanical

strength must be considered when designing and selecting filament materials.

4.2. Effects of processing parameters on voids

4.2.1. Nozzle temperature
The nozzle temperature is critical for the print quality of FFF parts as it determines melt printability, raster bonding and feedstock degradation. Spoerk et al. found that increased nozzle temperatures improved adhesion and resulted in smaller voids [38]. As shown in Fig. 9e [96], the PLA part printed at 245 °C exhibited fewer and smaller voids compared to that printed at 205 °C. Moreover, in the study by Wang et al. [72], although voids were clearly present on the cross-section of the PEEK part printed at 380 °C, voids were almost eliminated at 440 °C.

In addition to decreased viscosity and increased flow-ability, higher nozzle temperatures also affect size accuracy and polymer thermal degradation. In the study by Gao et al. [78], void size in cross-section of the PA 1012 part decreased gradually with the increase of nozzle temperature. However, air bubbles became more prevalent as the printing temperature reached 260 °C. Although void presence was greatly reduced by the higher nozzle temperature, the thermal degradation of PA 1012 could negatively impact the parts mechanical properties.

4.2.2. Bed/plate temperature
Print bed temperature has been found to be a relevant parameter in void formation along the Z-axis [26,77]. Print bed temperature is commonly higher than the glass transition temperature (T_g) of feedstock [77]. Sufficient energy from the print bed keeps the polymer at their glassy phase, which facilitates molecular chain movement. In the study by Aliheidari et al. [77], smaller voids were observed in parts (Fig. 10) printed at higher bed temperatures. However, print bed temperature loses effectiveness further away from the print bed. As it can be seen in Fig. 9e, the voids in each layer gradually grew in size along the Z-axis [96]. Nevertheless, an appropriate print bed temperature suitable for the corresponding feedstock is desirable for obtaining relatively isotropic printed structures.

4.2.3. Printing speed
Fresh, hot extrudates could transfer heat to nearby deposited rasters and supply energy for interface welding. Holding filament feed speed and nozzle temperature constant, the melting duration of feedstock in the print head is determined by printing speed. Higher printing speeds translate into
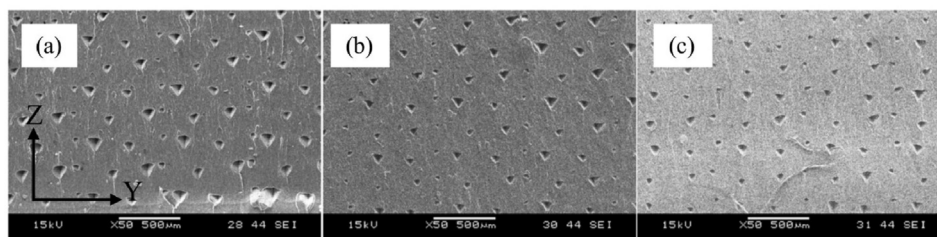

Fig. 10 – Cross-sections of FFF parts at bed temperatures of (a) 85 °C, (b) 95 °C and (c) 105 °C. Z is the height direction [77].
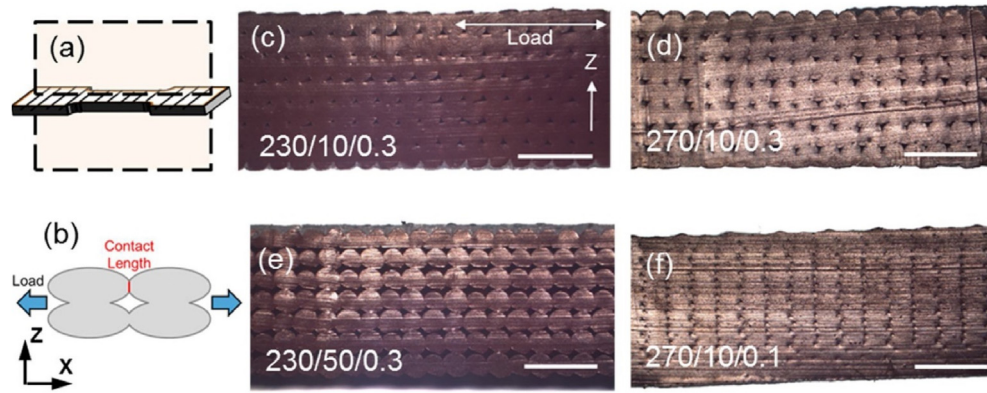
Fig. 11 — Comparison of mesostructures: (a) Part printed in XY orientation; (b) Schematic cross section; (c—f) Select mesostructures of parts printed with parameters shown as nozzle temperature/printing speed/layer height. Scale bar = 1 mm [71].

smaller windows for heat transfer, which may result in the extrusion of partial melted extrudate. During deposition, the amount of time extrudates retain temperatures above the T_g of feedstock has been found to be inversely proportional to printing speed. Therefore, the longer contact time from slower printing speeds could facilitate interface welding. As shown in Fig. 11c and e, at a nozzle temperature of 230 °C, compared to parts printed at 10 mm/s, Abbott et al. observed larger voids in parts printed at 50 mm/s [71]. In addition, increases in printing speed has been found to increase void presence and decrease density in FFF PEEK parts [72].

Simulations conducted by Wang et al. [72] demonstrated that printing speed influences the feedstock melted state. Higher printing speeds resulted in parts with greater void quantity and worsened interlayer bonding. Moreover, printing at higher speeds could affect polymer crystallization. Small partially melted polymer particles may act as nucleation sites and further constrain interface diffusion [29]. In summary, although effective at decreasing void fraction and facilitating interlayer bonding, lowering printing speed means sacrificing build time and printing efficiency. Therefore, it is crucial to balance print productivity and quality when adjusting printing speed.

4.2.4. Layer size

Layer height and raster width are two key parameters to consider when optimizing FFF prints. Layer height is a determinant for slicing and build time, while raster width affects raster contact. Holding all other print parameters constant, layer height has been found to influence the heating history of rasters and interlayer bonding. Aliheidari et al. [77] found that printing with a layer height of 0.2 mm yielded ABS parts with superior mechanical performance than layer heights of 0.1 mm and 0.3 mm. Notably, a layer height of 0.1 mm resulted in increased neck length between neighboring rasters and smaller inter-layer voids. However, as a result of the thinner layers, the consequential faster cooling rate further reduced the extrudes welding abilities and weakened interface bonding. For layers of 0.1 mm, the increase of thermally driven heating—cooling cycles in rasters induced undesirable residual stress accumulation, resulting in additional microdefects

and degraded mechanical properties [77]. Surprisingly, increasing layer height to 0.3 mm dramatically increased void size. This phenomenon in prints with thicker layers could be explained by the reduction of contact pressure applied to the bottom layer as a result of the shorter neck length, as shown in Fig. 12a [77]. In Fig. 12b, pressure within extruded fibers is shown to increase exponentially for layers thinner than 0.2 mm [99]. Therefore, higher exiting pressures may facilitate interface contact [100]. Similar relationships between void
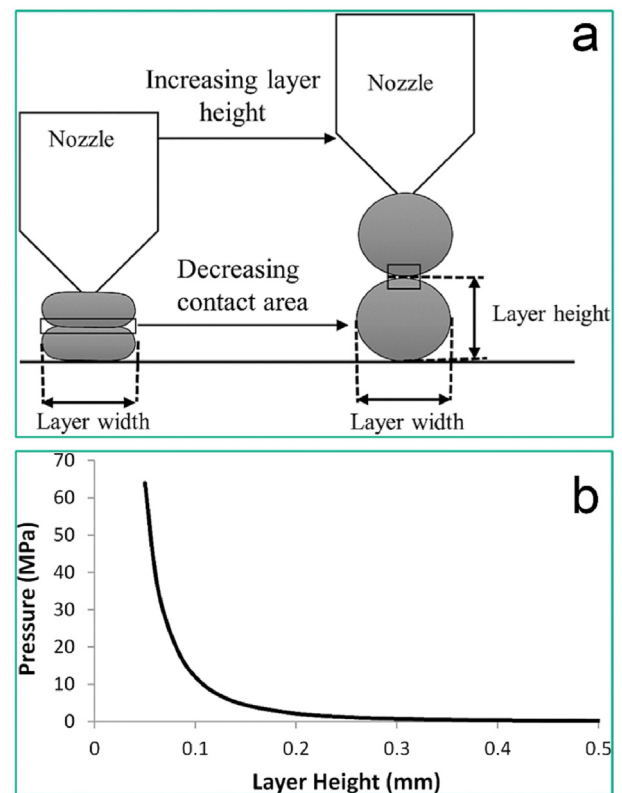

Fig. 12 — (a) Neck length varies with layer height [77]; (b) Pressure within the extruded fibers drops with the increase of layer height [99].

morphology and layer height have been observed in parts printed with PLA [26], PP [75] and ABS [71], as shown in Fig. 11d and f.

Raster width determines the distance between rasters and, therefore, affects void formation. Increased raster width results in a larger contact area and fewer voids [77,101]. Larger raster overlap is beneficial for interface diffusion and welding. Rajpurohit et al. [101] compared the morphology and impact strength of PLA parts printed at raster widths of 0.5 mm, 0.6 mm and 0.7 mm. Their results demonstrated that prints with larger raster width contained smaller voids and exhibited higher impact strengths as a result of smoother raster contact. In general, the higher thermal transfer and larger contact areas of wider rasters enhance their ability to retain temperatures above T_g. Consequently, a longer duration in the appropriate temperature conditions enables more complete interface diffusion and welding [99,100].

4.2.5. Infill pattern and density

A selection of infill patterns aiming at reducing material usage and print weight could be found in common FFF slicers. For instance, there are 13 user-selectable infill patterns in the Ultimaker Cura (4.10) software, including grid, lines, triangles, tri-hexagon, cubic, cubic subdivision, octet, quarter cubic, concentric, zig-zag, cross, cross 3D, concentric 3D and gyroid. The internal geometry of FFF parts is designable by adjusting infill patterns and infill densities. Naturally, void fraction increases with the decrease of infill density. As shown in Fig. 13, the infill pattern determines void distribution and morphology in prints with the same infill density. Moreover, the arrangement and orientation of rasters in distinct infill patterns could impose varying degrees of influence on the thermal history of neighbor rasters, which would impact interface strength and collapse mode [102]. Aloyaydi et al. investigated the low-velocity impact performance of parts printed with triangle, grid, quarter cube and tri-hexagon infill patterns. The triangle infill was found to possess the highest energy absorption capacity and stiffness [73]. While all specimens were printed with a 60% infill density, more contact layers orthogonal to the impactor and fewer voids lent prints with the triangle infill higher impact resistance. As for compression performance, effective layer contacts in the
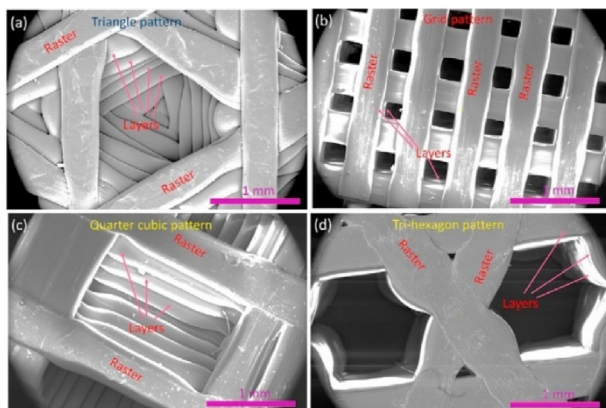
Fig. 13 − SEM images of FFF specimens with (a) triangle; (b) grid; (c) quarter cube; (d) tri-hexagon infill pattern [73].
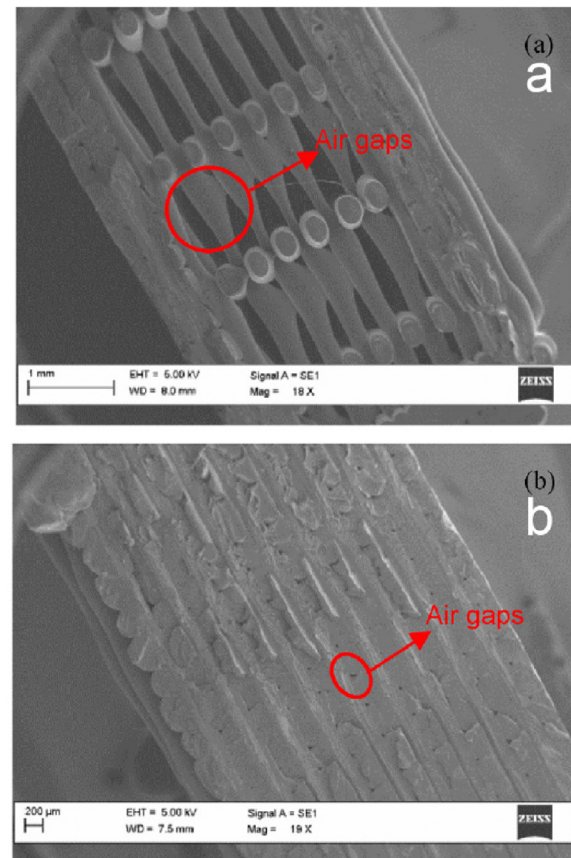
Fig. 14 − Voids (air gaps in red) of fractured PLA samples: (a) 25% infill density; (b) 100% infill density [74].

direction of compressive loading enabled the grid pattern to endure the highest compressive strength at 72 MPa. Furthermore, in the study by Mishra et al. [103], comparisons between the impact capacity of the twelve aforementioned infill patterns (except for the gyroid pattern) revealed that the line, zigzag and concentric infills absorbed more impact energy when printed at infill densities of 50% and 75%. In summary, different infill patterns contain distinct inter-layer and raster connections, which would affect stress distribution and dissipation. Therefore, the infill pattern used in FFF prints should be appropriate for corresponding mechanical requirements.

Infill density impacts the amount of feedstock used in FFF parts. Printing with smaller infill density yields lighter products. Naturally, void size is directly correlated with infill density, as shown in Fig. 14 [74]. Samples printed with 100% infill density contained voids minimal in size. Therefore, increasing infill density is a promising method for reducing void fraction and improving tensile modulus [74]. As for impact properties, 85% was found to be the optimal infill density for line, zigzag and concentric infills in the study by Mishra et al. [103]. Infill density also impacts the tensile and flexural strengths of FFF parts. The highest flexural strength was achieved when printing with 100% infill for the concentric, Hilbert curve, rectilinear and honeycomb patterns [102].
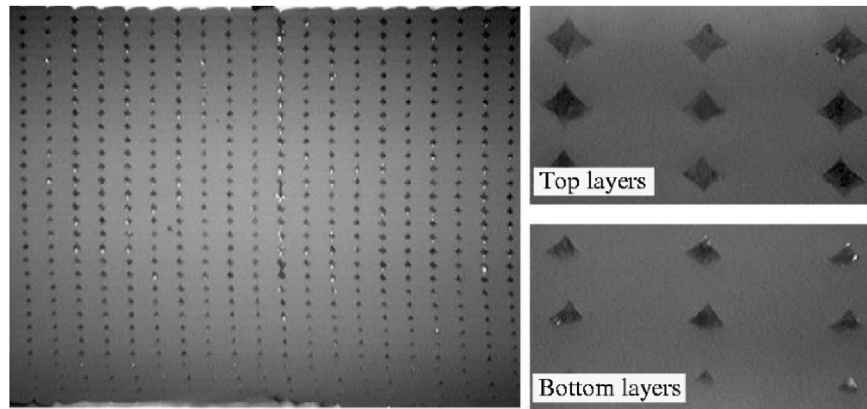
Fig. 15 – Cross-sectional morphology of a 30-layer FFF part [63].

4.2.6. *Position on the Z axis*

The thermal history of rasters is a key factor that affects layer and raster bonding [71]. The position of the part on the print bed and/or the distance from each layer to the print bed have been found to influence the thermal history of rasters. The temperature gradient along the build direction varies between each subsequent layer. Therefore, void heterogeneity in parts is stronger in layers closer to the print bed. In Fig. 15, void size visibly grows from bottom to top in the 30-layer part. Holding other printing parameters constant, the duration rasters retain temperatures above T_g is dependent on the print bed and ambient environmental temperatures. Notably, Coogan et al. found that the weakest zones of tensile strength in specimens were the furthest from the heated print bed [100]. In summary, maintaining an appropriate environmental temperature is a promising way to maximize temperature homogeneity in parts.

4.3. *Experimental design in fused filament fabrication*

Printing parameters have great influence on the properties of FFF printed parts. The design of experiments (DoE), also known as experimental design, is critical for effectively fine-tuning the numerous printing parameters necessary for high-quality prints [105,106]. DoE's statistical optimization strategies have been found to be effective in obtaining ideal formulations [107–109], processes [110], methods [105] and products [111]. Factors such as the nozzle temperature, print bed temperature, printing speed and layer size affect the void formation and mechanical performance of printed parts. The OFAT (One Factor At a Time) approach is commonly used for determining a suitable set of FFF printing parameters [74,77,110,112]. However, as OFAT assumes that printing parameter effects are fully independent, achieving true optimality has proven to be challenging and time-consuming. Conversely, DoE offers techniques capable of exploring a much larger experimental domain with superior efficiency and efficacy [106]. Nevertheless, the OFAT approach is a reliable method used for screening factors of significance and setting initial factor levels before conducing DoE procedures.

DoE is efficient in analyzing the effects of printing parameters on the dimension accuracy, density variation and mechanical properties of FFF printed parts. The literature related to DoE are summarized in Table 4. Factorial designs such as full factorial design, centered central composite design, mixture design and Box-Behnken design [38,71,101,113–118] are used for evaluating the geometric accuracy, interlayer bonds, density and mechanical properties of prints. Although few studies employ DoE for FFF void characterization, full factorial design has been proven to be an effective technique for evaluating voids in parts printed by direct ink writing [119]. Taguchi design is another useful method for optimizing nozzle diameter, infill density, printing speed and layer height to achieve superior fatigue evaluation, minimum weight and minimum printing time [120,121]. Evidently, parameters such as infill density and properties such as mechanical performance and fatigue have direct connections to void presence. Therefore, DoE is a feasible method for establishing the link between printing parameters and FFF voids.

The constant emergence of new feedstocks and myriads customized products put increasing pressure on the demand for speed and efficiency when optimizing 3D printing parameters. As an alternate for DoE, machine learning (ML) is a method for rapidly processing experimental data [122–124]. ML has been used for processing parameter optimization, porosity prediction and defect detection in 3D printed parts [123]. Artificial neural networks (ANN) are also commonly used to analyze the 3D printing process. As shown in Table 4, ANN was chosen to optimize product appearance [125,126], production-cost-dependent variables and mechanical performance, such as toughness [127], tensile strength [128], compressive stress [129], sliding wear [130] and viscoelastic responses [131,132]. Although current research on void analysis, void prediction and defect detection with ML is primarily focused on laser additive manufacturing [123], the core analysis concepts are compatible with FFF. Evidently, much regarding the analysis of FFF voids and prints with ML has yet to be explored.

Table 4 – The use of experimental design in the optimization of FFF parameters.

Method	Target attributes	Factors	Numbers of factor level	Ref.
Full factorial design	Interlayer bond strength	Nozzle temperature, printing speed, layer height, building orientation	2	[71]
	Impact strength	Raster angle, layer height, raster width	3	[101]
	Geometric accuracy	Feed rate, nozzle temperature, flow rate, layer height, infill density	3	[113]
	Mechanical properties	Layer height, raster pattern, infill density	2	[114]
	Filament geometry, inter-filament void formation	Layer height, extrusion rate, printing speed, nozzle diameter	2	[119]
Mixed-level factorial design	Inter- and intra-layer strengths	Nozzle temperature, layer height, layer density	Mixed-level	[38]
Half fractional design	Printing time, energy consumption, surface roughness, dimensional accuracy	Layer height, infill density, nozzle temperature, number of shells, printing speed, retraction speed	2	[115]
Face-centered central composite design	Compressive stress, breaking stress, deformation	Raster angle, air gap, raster width	3	[118]
Central composite design	Tensile strength, parts weight, elongation at break, build time	Layer height, infill density, number of contours	5	[116]
Taguchi design	Mechanical properties, part weight, printing time	Infill density, printing speed, layer height	Mixed-level	[120]
	Fatigue life	Layer height, infill density, nozzle diameter, extrusion rate	3	[121]
Box-Behnken Design	Density, building time, surface roughness, micro-hardness	Infill density, layer height, bed temperature	3	[117]
ANN	Dimensional accuracy	Layer height, building orientation, air gap, raster angle, raster width	3	[125]
	Surface roughness	Nozzle temperature, layer height, printing speed	3	[126]
	Toughness, part thickness, production-cost-dependent variables	Nozzle temperature, infill density, layer height	5	[127]
	Tensile strength	Nozzle temperature, layer height, raster pattern orientation	Mixed-level	[128]
	Compressive stress	Layer height, building orientation, raster angle, raster width, air gap	3	[129]
	Sliding wear	Layer height, building orientation, raster angle, raster width, air gap	3	[130]
	Viscoelastic responses	Layer height, air gap, build orientation, raster angle, road width, number of contours	3	[131]
	Dynamic modulus of elasticity	Layer height, air gap, raster angle, build orientation, raster width, number of contours	2	[132]

5.   Conclusions

Despite recent advancements, much about void presence in FFF printed parts remains unknown. In summary, imaging is the primary experimental method utilized by existing studies to inspect and analyze existing void structures. Although SEM, OM and μCT imaging have yielded promising results, there exist shortcomings in the current state of FFF void research:

(1) As seen in Table 3, the effects of feedstocks and printing parameters on voids are not comprehensive.
(2) The three-dimensional structural characterization of the voids is not clear.

These unknowns hinder FFF ability to prepare polymer parts with specific hierarchical structures and optimal mechanical performance. Therefore, FFF void structures should be further studied.

(3) Void presence could affect interlayer thermal transfer and thus further weak the interlayer bonding, which might create additional voids. This potential process of void formation and feedback has not been investigated.

(4) The characteristics of void structures could reveal valuable information for implementing and/or improving treatments designed to improve part strength, such as post annealing or impregnation with other phases. Voids in printed parts form channels for heat and mass transfer. The utilization of voids as channels for heat and mass transfer should be further investigated in future.

(5) Although the relationship between voids and the mechanical performance of FFF parts have been investigated by many researchers, the effects of voids on dynamic mechanical properties and fatigue performance are seldomly discussed.

(6) Compared to pure polymer materials, composite feedstocks with organic or inorganic fillers generally exhibit different properties, such as die swell, heat transfer and crystallization. There remains a need for more information regarding the details of void formation in parts printed with composite feedstocks.

Declaration of Competing Interest

The authors declare that they have no known competing financial interests or personal relationships that could have appeared to influence the work reported in this paper.

Acknowledgments

REFERENCES

[1] ISO/ASTM52900-15. Standard terminology for additive manufacturing-general principles- terminology. West Conshohocken, PA: ASTM International; 2015. https://doi.org/10.1520/ISOASTM52900-15.

[2] Tao Y, Yin Q, Li P. An additive manufacturing method using large-scale wood inspired by laminated Object manufacturing and Plywood technology. Polym Basel 2021;13:144. https://doi.org/10.3390/polym13010144.

[3] Tofail SAM, Koumoulos EP, Bandyopadhyay A, Bose S, Donoghue LO, Charitidis C. Additive manufacturing: scientific and technological challenges, market uptake and opportunities. Mater Today 2018;21:22–37. https://doi.org/10.1016/j.mattod.2017.07.001.

[4] Gao X, Qi S, Kuang X, Su Y, Li J, Wang D. Fused filament fabrication of polymer materials: a review of interlayer bond. Addit Manuf 2020:101658. https://doi.org/10.1016/j.addma.2020.101658.

[5] Daminabo SC, Goel S, Grammatikos SA, Nezhad HY, Thakur VK. Fused deposition modeling-based additive manufacturing (3D printing): techniques for polymer material systems. Mater Today Chem 2020;16:100248. https://doi.org/10.1016/j.mtchem.2020.100248.

[6] Tao Y, Liu M, Han W, Li P. Waste office paper filled polylactic acid composite filaments for 3D printing. Compos B Eng 2021;221:108998. https://doi.org/10.1016/j.compositesb.2021.108998.

[7] Rafiee M, Farahani RD, Therriault D. Multi-material 3D and 4D printing: a survey. Adv Sci 2020;7:1902307. https://doi.org/10.1002/advs.201902307.

[8] Friedrich L, Begley M. Printing direction dependent microstructures in direct ink writing. Addit Manuf 2020;34:101192. https://doi.org/10.1016/j.addma.2020.101192.

[9] Diener S, Franchin G, Achilles N, Kuhnt T, Rösler F, Katsikis N, et al. X-ray microtomography investigations on the residual pore structure in silicon nitride bars manufactured by direct ink writing using different printing patterns. Open Ceram 2021;5:100042. https://doi.org/10.1016/j.oceram.2020.100042.

[10] Buswell RA, Leal De Silva WR, Jones SZ, Dirrenberger J. 3D printing using concrete extrusion: a roadmap for research. Cement Concr Res 2018;112:37–49. https://doi.org/10.1016/j.cemconres.2018.05.006.

[11] Serdeczny MP, Comminal R, Pedersen DB, Spangenberg J. Numerical simulations of the mesostructure formation in material extrusion additive manufacturing. Addit Manuf 2019;28:419–29. https://doi.org/10.1016/j.addma.2019.05.024.

[12] Turner BN, Strong R, Gold SA. A review of melt extrusion additive manufacturing processes: I. Process design and modeling. Rapid Prototyp J 2014;20:192–204. https://doi.org/10.1108/RPJ-01-2013-0012.

[13] Ngo TD, Kashani A, Imbalzano G, Nguyen KTQ, Hui D. Additive manufacturing (3D printing): a review of materials, methods, applications and challenges. Compos B Eng 2018;143:172–96. https://doi.org/10.1016/j.compositesb.2018.02.012.

[14] Tao Y, Li P, Pan L. Improving tensile properties of polylactic acid parts by adjusting printing parameters of open source 3D printers. Mater Sci (MEDŽIAGOTYRA) 2020;25:83–7. https://doi.org/10.5755/j01.ms.26.1.20952.

[15] Wu H, Fahy WP, Kim S, Kim H, Zhao N, Pilato L, et al. Recent developments in polymers/polymer nanocomposites for additive manufacturing. Prog Mater Sci 2020;111:100638. https://doi.org/10.1016/j.pmatsci.2020.100638.

[16] Brenken B, Barocio E, Favaloro A, Kunc V, Pipes RB. Fused filament fabrication of fiber-reinforced polymers: a review. Addit Manuf 2018;21:1–16. https://doi.org/10.1016/j.addma.2018.01.002.

[17] Zhao X, Tekinalp H, Meng X, Ker D, Benson B, Pu Y, et al. Poplar as biofiber reinforcement in composites for large-scale 3D printing. ACS Appl Bio Mater 2019;2:4557–70. https://doi.org/10.1021/acsabm.9b00675.

[18] Espalin D, Alberto RJ, Medina F, Wicker R. Multi-material, multi-technology FDM: exploring build process variations. Rapid Prototyp J 2014;20:236–44. https://doi.org/10.1108/RPJ-12-2012-0112.

[19] Singh S, Singh G, Prakash C, Ramakrishna S. Current status and future directions of fused filament fabrication. J Manuf Process 2020;55:288–306. https://doi.org/10.1016/j.jmapro.2020.04.049.

[20] Najmon JC, Raeisi S, Tovar A. Review of additive manufacturing technologies and applications in the aerospace industry. In: Froes F, Boyer R, editors. Additive

manufacturing for the aerospace industry. Amsterdam: Elsevier; 2019. p. 7—31. https://doi.org/10.1016/B978-0-12-814062-8.00002-9.

[21] Placone JK, Engler AJ. Recent advances in extrusion-based 3D printing for biomedical applications. Adv Healthcare Mater 2018;7:1701161. https://doi.org/10.1002/adhm.201701161.

[22] Mohd Pu 'Ad NAS, Abdul Haq RH, Mohd Noh H, Abdullah HZ, Idris MI, Lee TC. Review on the fabrication of fused deposition modelling (FDM) composite filament for biomedical applications. Mater Today: Proc 2020;29:228—32. https://doi.org/10.1016/j.matpr.2020.05.535.

[23] Christ JF, Aliheidari N, Ameli A, Pötschke P. 3D printed highly elastic strain sensors of multiwalled carbon nanotube/thermoplastic polyurethane nanocomposites. Mater Des 2017;131:394—401. https://doi.org/10.1016/j.matdes.2017.06.011.

[24] Yadav DK, Srivastava R, Dev S. Design & fabrication of ABS part by FDM for automobile application. Mater Today: Proc 2020;26:2089—93. https://doi.org/10.1016/j.matpr.2020.02.451.

[25] Peterson AM. Review of acrylonitrile butadiene styrene in fused filament fabrication: a plastics engineering-focused perspective. Addit Manuf 2019;27:363—71. https://doi.org/10.1016/j.addma.2019.03.030.

[26] Wang L, Gramlich WM, Gardner DJ. Improving the impact strength of poly (lactic acid) (PLA) in fused layer modeling (FLM). Polymer 2017;114:242—8. https://doi.org/10.1016/j.polymer.2017.03.011.

[27] Liu Z, Wang Y, Wu B, Cui C, Guo Y, Yan C. A critical review of fused deposition modeling 3D printing technology in manufacturing polylactic acid parts. Int J Adv Manuf Technol 2019;102:2877—89. https://doi.org/10.1007/s00170-019-03332-x.

[28] Tao Y, Wang H, Li Z, Li P, Shi SQ. Development and application of wood flour-filled polylactic acid composite filament for 3D printing. Materials 2017;10:339. https://doi.org/10.3390/ma10040339.

[29] Vaes D, Van Puyvelde P. Semi-crystalline feedstock for filament-based 3D printing of polymers. Prog Polym Sci 2021;118:101411. https://doi.org/10.1016/j.progpolymsci.2021.101411.

[30] Ligon SC, Liska R, Stampfl J, Gurr M, Mülhaupt R. Polymers for 3D printing and customized additive manufacturing. Chem Rev 2017;117:10212—90. https://doi.org/10.1021/acs.chemrev.7b00074.

[31] Dawoud M, Taha I, Ebeid SJ. Mechanical behaviour of ABS: an experimental study using FDM and injection moulding techniques. J Manuf Process 2016;21:39—45. https://doi.org/10.1016/j.jmapro.2015.11.002.

[32] Xiao X, Chevali VS, Song P, He D, Wang H. Polylactide/hemp hurd biocomposites as sustainable 3D printing feedstock. Compos Sci Technol 2019;184:107887. https://doi.org/10.1016/j.compscitech.2019.107887.

[33] Ahn SH, Montero M, Odell D, Roundy S, Wright PK. Anisotropic material properties of fused deposition modeling ABS. Rapid Prototyp J 2002;8:248—57. https://doi.org/10.1108/13552540210441166.

[34] Turner BN, Gold SA. A review of melt extrusion additive manufacturing processes: II. Materials, dimensional accuracy and surface roughness. Rapid Prototyp J 2015;21:250—61. https://doi.org/10.1108/RPJ-02-2013-0017.

[35] Alafaghani A, Qattawi A, Ablat MA. Design consideration for additive manufacturing: fused deposition modelling. Open J Appl Sci 2017;7:291—318. https://doi.org/10.4236/ojapps.2017.76024.

[36] Karakurt I, Lin L. 3D printing technologies: techniques, materials and post-processing. Curr Opin Chem Eng 2020;28:134—43. https://doi.org/10.1016/j.coche.2020.04.001.

[37] Mackay ME. The importance of rheological behavior in the additive manufacturing technique material extrusion. J Rheol 2018;62:1549—61. https://doi.org/10.1122/1.5037687.

[38] Spoerk M, Arbeiter F, Cajner H, Sapkota J, Holzer C. Parametric optimization of intra- and inter-layer strengths in parts produced by extrusion-based additive manufacturing of poly(lactic acid). J Appl Polym Sci 2017;134:45401. https://doi.org/10.1002/app.45401.

[39] van de Werken N, Tekinalp H, Khanbolouki P, Ozcan S, Williams A, Tehrani M. Additively manufactured carbon fiber-reinforced composites: state of the art and perspective. Addit Manuf 2020;31:100962. https://doi.org/10.1016/j.addma.2019.100962.

[40] Hu C, Qin Q. Advances in fused deposition modeling of discontinuous fiber/polymer composites. Curr Opin Solid St M 2020;24:100867. https://doi.org/10.1016/j.cossms.2020.100867.

[41] Penumakala PK, Santo J, Thomas A. A critical review on the fused deposition modeling of thermoplastic polymer composites. Compos B Eng 2020;201:108336. https://doi.org/10.1016/j.compositesb.2020.108336.

[42] Bellehumeur C, Li L, Sun Q, Gu P. Modeling of bond formation between polymer filaments in the fused deposition modeling process. J Manuf Process 2004;6:170—8. https://doi.org/10.1016/S1526-6125(04)70071-7.

[43] Rodríguez JF, Thomas JP, Renaud JE. Mechanical behavior of acrylonitrile butadiene styrene fused deposition materials modeling. Rapid Prototyp J 2003;9:219—30. https://doi.org/10.1108/13552540310489604.

[44] Kio OJ, Yuan J, Brooks AJ, Knapp GL, Ham K, Ge J, et al. Non-destructive evaluation of additively manufactured polymer objects using X-ray interferometry. Addit Manuf 2018;24:364—72. https://doi.org/10.1016/j.addma.2018.04.014.

[45] Rodriguez JF, Thomas JP, Renaud JE. Characterization of the mesostructure of fused-deposition acrylonitrile-butadiene-styrene materials. Rapid Prototyp J 2000;6:175—86. https://doi.org/10.1108/13552540010337056.

[46] Alaimo G, Marconi S, Costato L, Auricchio F. Influence of meso-structure and chemical composition on FDM 3D-printed parts. Compos B Eng 2017;113:371—80. https://doi.org/10.1016/j.compositesb.2017.01.019.

[47] Koch C, Van Hulle L, Rudolph N. Investigation of mechanical anisotropy of the fused filament fabrication process via customized tool path generation. Addit Manuf 2017;16:138—45. https://doi.org/10.1016/j.addma.2017.06.003.

[48] Chin AK, Fai LK, Kai CC, Chandrasekaran M. Investigation of the mechanical properties and porosity relationships in fused deposition modelling-fabricated porous structures. Rapid Prototyp J 2006;12:100—5. https://doi.org/10.1108/13552540610652447.

[49] Gleadall A, Ashcroft I, Segal J. VOLCO: a predictive model for 3D printed microarchitecture. Addit Manuf 2018;21:605—18. https://doi.org/10.1016/j.addma.2018.04.004.

[50] Bekas DG, Hou Y, Liu Y, Panesar A. 3D printing to enable multifunctionality in polymer-based composites: a review. Compos B Eng 2019;179:107540. https://doi.org/10.1016/j.compositesb.2019.107540.

[51] Liu Y, Zhang W, Zhang F, Leng J, Pei S, Wang L, et al. Microstructural design for enhanced shape memory behavior of 4D printed composites based on carbon nanotube/polylactic acid filament. Compos Sci Technol 2019;181:107692. https://doi.org/10.1016/j.compscitech.2019.107692.

[52] Le Duigou A, Castro M, Bevan R, Martin N. 3D printing of wood fibre biocomposites: from mechanical to actuation

functionality. Mater Des 2016;96:106–14. https://doi.org/10.1016/j.matdes.2016.02.018.

[53] Compton BG, Lewis JA. 3D-Printing of lightweight cellular composites. Adv Mater 2014;26:5930–5. https://doi.org/10.1002/adma.201401804.

[54] Shanmugam V, Das O, Babu K, Marimuthu U, Veerasimman A, Johnson DJ, et al. Fatigue behaviour of FDM-3D printed polymers, polymeric composites and architected cellular materials. Int J Fatig 2021;143:106007. https://doi.org/10.1016/j.ijfatigue.2020.106007.

[55] Bellini A, Güçeri S. Mechanical characterization of parts fabricated using fused deposition modeling. Rapid Prototyp J 2003;9:252–64. https://doi.org/10.1108/13552540310489631.

[56] Guessasma S, Belhabib S, Nouri H. Effect of printing temperature on microstructure, thermal behavior and tensile properties of 3D printed nylon using fused deposition modeling. J Appl Polym Sci 2021;138:50162. https://doi.org/10.1002/app.50162.

[57] Mohamed OA, Masood SH, Bhowmik JL. Optimization of fused deposition modeling process parameters: a review of current research and future prospects. Adv Manuf 2015;3:42–53. https://doi.org/10.1007/s40436-014-0097-7.

[58] Rahim TNAT, Abdullah AM, Md Akil H. Recent developments in fused deposition modeling-based 3D printing of polymers and their composites. Polym Rev 2019;59:589–624. https://doi.org/10.1080/15583724.2019.1597883.

[59] Tao Y, Pan L, Liu D, Li P. A case study: mechanical modeling optimization of cellular structure fabricated using wood flour-filled polylactic acid composites with fused deposition modeling. Compos Struct 2019;216:360–5. https://doi.org/10.1016/j.compstruct.2019.03.010.

[60] Rezayat H, Zhou W, Siriruk A, Penumadu D, Babu SS. Structure-mechanical property relationship in fused deposition modelling. Mater Sci Technol 2015;31:895–903. https://doi.org/10.1179/1743284715Y.0000000010.

[61] Gurrala PK, Regalla SP. Part strength evolution with bonding between filaments in fused deposition modelling. Virtual Phys Prototyp 2014;9:141–9. https://doi.org/10.1080/17452759.2014.913400.

[62] Li L, Sun Q, Bellehumeur C, Gu P. Composite modeling and analysis for fabrication of FDM prototypes with locally controlled properties. J Manuf Process 2002;4:129–41. https://doi.org/10.1016/S1526-6125(02)70139-4.

[63] Sun Q, Rizvi GM, Bellehumeur CT, Gu P. Effect of processing conditions on the bonding quality of FDM polymer filaments. Rapid Prototyp J 2008;14:72–80. https://doi.org/10.1108/13552540810862028.

[64] Seppala JE, Hoon Han S, Hillgartner KE, Davis CS, Migler KB. Weld formation during material extrusion additive manufacturing. Soft Matter 2017;13:6761–9. https://doi.org/10.1039/C7SM00950J.

[65] Polychronopoulos ND, Vlachopoulos J. The role of heating and cooling in viscous sintering of pairs of spheres and pairs of cylinders. Rapid Prototyp J 2020;26:719–26. https://doi.org/10.1108/RPJ-06-2019-0162.

[66] Bhalodi D, Zalavadiya K, Gurrala PK. Influence of temperature on polymer parts manufactured by fused deposition modeling process. J Braz Soc Mech Sci 2019;41:113. https://doi.org/10.1007/s40430-019-1616-z.

[67] Huang B, Singamneni S. Raster angle mechanics in fused deposition modelling. J Compos Mater 2014;49:363–83. https://doi.org/10.1177/0021998313519153.

[68] Agarwala MK, Jamalabad VR, Langrana NA, Safari A, Whalen PJ, Danforth SC. Structural quality of parts processed by fused deposition. Rapid Prototyp J 1996;2:4–19. https://doi.org/10.1108/13552549610732034.

[69] Tekinalp HL, Kunc V, Velez-Garcia GM, Duty CE, Love LJ, Naskar AK, et al. Highly oriented carbon fiber-polymer composites via additive manufacturing. Compos Sci Technol 2014;105:144–50. https://doi.org/10.1016/j.compscitech.2014.10.009.

[70] Downing D, Jones A, Brandt M, Leary M. Increased efficiency gyroid structures by tailored material distribution. Mater Des 2021;197:109096. https://doi.org/10.1016/j.matdes.2020.109096.

[71] Abbott AC, Tandon GP, Bradford RL, Koerner H, Baur JW. Process-structure-property effects on ABS bond strength in fused filament fabrication. Addit Manuf 2018;19:29–38. https://doi.org/10.1016/j.addma.2017.11.002.

[72] Wang P, Zou B, Xiao H, Ding S, Huang C. Effects of printing parameters of fused deposition modeling on mechanical properties, surface quality and microstructure of PEEK. J Mater Process Technol 2019;271:62–74. https://doi.org/10.1016/j.jmatprotec.2019.03.016.

[73] Aloyaydi B, Sivasankaran S, Mustafa A. Investigation of infill-patterns on mechanical response of 3D printed poly-lactic-acid. Polym Test 2020;87:106557. https://doi.org/10.1016/j.polymertesting.2020.106557.

[74] Abeykoon C, Sri-Amphorn P, Fernando A. Optimization of fused deposition modeling parameters for improved PLA and ABS 3D printed structures. Int J Lightweight Mater Manuf 2020;3:284–97. https://doi.org/10.1016/j.ijlmm.2020.03.003.

[75] Wang L, Gardner DJ. Effect of fused layer modeling (FLM) processing parameters on impact strength of cellular polypropylene. Polymer 2017;113:74–80. https://doi.org/10.1016/j.polymer.2017.02.055.

[76] Gao X, Zhang D, Wen X, Qi S, Su Y, Dong X. Fused deposition modeling with polyamide 1012. Rapid Prototyp J 2019;25:1145–54. https://doi.org/10.1108/RPJ-09-2018-0258.

[77] Aliheidari N, Christ J, Tripuraneni R, Nadimpalli S, Ameli A. Interlayer adhesion and fracture resistance of polymers printed through melt extrusion additive manufacturing process. Mater Des 2018;156:351–61. https://doi.org/10.1016/j.matdes.2018.07.001.

[78] Gao X, Qi S, Zhang D, Su Y, Wang D. The role of poly (ethylene glycol) on crystallization, interlayer bond and mechanical performance of polylactide parts fabricated by fused filament fabrication. Addit Manuf 2020;35:101414. https://doi.org/10.1016/j.addma.2020.101414.

[79] Levenhagen NP, Dadmun MD. Bimodal molecular weight samples improve the isotropy of 3D printed polymeric samples. Polymer 2017;122:232–41. https://doi.org/10.1016/j.polymer.2017.06.057.

[80] Guessasma S, Belhabib S, Nouri H. Microstructure and mechanical performance of 3D printed wood-PLA/PHA using fused deposition modelling: effect of printing temperature. Polym Basel 2019;11:1778. https://doi.org/10.3390/polym11111778.

[81] Guessasma S, Belhabib S, Nouri H. Understanding the microstructural role of bio-sourced 3D printed structures on the tensile performance. Polym Test 2019;77:105924. https://doi.org/10.1016/j.polymertesting.2019.105924.

[82] Guessasma S, Belhabib S, Nouri H. Printability and tensile performance of 3D Printed polyethylene terephthalate glycol using fused deposition modelling. Polym Basel 2019;11:1220. https://doi.org/10.3390/polym11071220.

[83] Guessasma S, Belhabib S, Nouri H. Microstructure, thermal and mechanical behavior of 3D printed acrylonitrile styrene

acrylate. Macromol Mater Eng 2019;304:1800793. https://doi.org/10.1002/mame.201800793.

[84] Hernandez-Contreras A, Ruiz-Huerta L, Caballero-Ruiz A, Moock V, Siller HR. Extended CT void analysis in FDM additive manufacturing components. Materials 2020;13:3831. https://doi.org/10.3390/ma13173831.

[85] Chisena RS, Engstrom SM, Shih AJ. Computed tomography evaluation of the porosity and fiber orientation in a short carbon fiber material extrusion filament and part. Addit Manuf 2020;34:101189. https://doi.org/10.1016/j.addma.2020.101189.

[86] Nouri H, Guessasma S, Belhabib S. Structural imperfections in additive manufacturing perceived from the X-ray micro-tomography perspective. J Mater Process Technol 2016;234:113–24. https://doi.org/10.1016/j.jmatprotec.2016.03.019.

[87] Yang D, Zhang H, Wu J, McCarthy ED. Fibre flow and void formation in 3D printing of short-fibre reinforced thermoplastic composites: an experimental benchmark exercise. Addit Manuf 2021;37:101686. https://doi.org/10.1016/j.addma.2020.101686.

[88] Sommacal S, Matschinski A, Drechsler K, Compston P. Characterisation of void and fiber distribution in 3D printed carbon-fiber/PEEK using X-ray computed tomography. Compos Part A Appl Sci Manuf 2021;149:106487. https://doi.org/10.1016/j.compositesa.2021.106487.

[89] Pokluda O, Bellehumeur CT, Vlachopoulos J. Modification of Frenkel's model for sintering. AIChE J 1997;43:3253–6. https://doi.org/10.1002/aic.690431213.

[90] Garzon-Hernandez S, Garcia-Gonzalez D, Jérusalem A, Arias A. Design of FDM 3D printed polymers: an experimental-modelling methodology for the prediction of mechanical properties. Mater Des 2020;188:108414. https://doi.org/10.1016/j.matdes.2019.108414.

[91] Das A, Gilmer EL, Biria S, Bortner MJ. Importance of polymer rheology on material extrusion additive manufacturing: correlating process physics to print properties. ACS Appl Polym Mater 2021;3:1218–49. https://doi.org/10.1021/acsapm.0c01228.

[92] Wang L, Palmer J, Tajvidi M, Gardner DJ, Han Y. Thermal properties of spray-dried cellulose nanofibril-reinforced polypropylene composites from extrusion-based additive manufacturing. J Therm Anal Calorim 2019;136:1069–77. https://doi.org/10.1007/s10973-018-7759-9.

[93] Ning F, Cong W, Qiu J, Wei J, Wang S. Additive manufacturing of carbon fiber reinforced thermoplastic composites using fused deposition modeling. Compos B Eng 2015;80:369–78. https://doi.org/10.1016/j.compositesb.2015.06.013.

[94] Parandoush P, Lin D. A review on additive manufacturing of polymer-fiber composites. Compos Struct 2017;182:36–53. https://doi.org/10.1016/j.compstruct.2017.08.088.

[95] Coogan TJ, Kazmer DO. Healing simulation for bond strength prediction of FDM. Rapid Prototyp J 2017;23:551–61. https://doi.org/10.1108/RPJ-03-2016-0051.

[96] Wolszczak P, Lygas K, Paszko M, Wach RA. Heat distribution in material during fused deposition modelling. Rapid Prototyp J 2018;24:615–22. https://doi.org/10.1108/RPJ-04-2017-0062.

[97] Ko YS, Herrmann D, Tolar O, Elspass WJ, Brändli C. Improving the filament weld-strength of fused filament fabrication products through improved interdiffusion. Addit Manuf 2019;29:100815. https://doi.org/10.1016/j.addma.2019.100815.

[98] Levenhagen NP, Dadmun MD. Interlayer diffusion of surface segregating additives to improve the isotropy of fused deposition modeling products. Polymer 2018;152:35–41. https://doi.org/10.1016/j.polymer.2018.01.031.

[99] Butler CA, Mccullough RL, Pitchumani R, Gillespie JW. An analysis of mechanisms governing fusion bonding of thermoplastic composites. J Thermoplast Compos 1998;11:338–63. https://doi.org/10.1177/089270579801100404.

[100] Coogan TJ, Kazmer DO. Bond and part strength in fused deposition modeling. Rapid Prototyp J 2017;23:414–22. https://doi.org/10.1108/RPJ-03-2016-0050.

[101] Rajpurohit SR, Dave HK. Impact strength of 3D printed PLA using open source FFF-based 3D printer. Prog Addit Manuf 2021;6:119–31. https://doi.org/10.1007/s40964-020-00150-6.

[102] Akhoundi B, Behravesh AH. Effect of filling pattern on the tensile and flexural mechanical properties of FDM 3D printed products. Exp Mech 2019;59:883–97. https://doi.org/10.1007/s11340-018-00467-y.

[103] Mishra PK, Senthil P, Adarsh S, Anoop MS. An investigation to study the combined effect of different infill pattern and infill density on the impact strength of 3D printed polylactic acid parts. Compos Commun 2021;24:100605. https://doi.org/10.1016/j.coco.2020.100605.

[104] Petersmann S, Spoerk-Erdely P, Feuchter M, Wieme T, Arbeiter F, Spoerk M. Process-induced morphological features in material extrusion-based additive manufacturing of polypropylene. Addit Manuf 2020;35:101384. https://doi.org/10.1016/j.addma.2020.101384.

[105] Hibbert DB. Experimental design in chromatography: a tutorial review. J Chromatogr B 2012;910:2–13. https://doi.org/10.1016/j.jchromb.2012.01.020.

[106] Mäkelä M. Experimental design and response surface methodology in energy applications: a tutorial review. Energy Convers Manag 2017;151:630–40. https://doi.org/10.1016/j.enconman.2017.09.021.

[107] Bella F, Pugliese D, Nair JR, Sacco A, Bianco S, Gerbaldi C, et al. A UV-crosslinked polymer electrolyte membrane for quasi-solid dye-sensitized solar cells with excellent efficiency and durability. Phys Chem Chem Phys 2013;15:3706–11. https://doi.org/10.1039/C3CP00059A.

[108] Pugliese D, Bella F, Cauda V, Lamberti A, Sacco A, Tresso E, et al. A chemometric approach for the sensitization procedure of ZnO flowerlike microstructures for Dye-Sensitized solar cells. Acs Appl Mater Inter 2013;5:11288–95. https://doi.org/10.1021/am403527m.

[109] Galliano S, Bella F, Bonomo M, Viscardi G, Gerbaldi C, Boschloo G, et al. Hydrogel electrolytes based on xanthan gum: green route towards stable dye-sensitized solar cells. Nanomaterials 2020;10:1585. https://doi.org/10.3390/nano10081585.

[110] Kaveh M, Badrossamay M, Foroozmehr E, Hemasian Etefagh A. Optimization of the printing parameters affecting dimensional accuracy and internal cavity for HIPS material used in fused deposition modeling processes. J Mater Process Technol 2015;226:280–6. https://doi.org/10.1016/j.jmatprotec.2015.07.012.

[111] Maqsood N, Rimašauskas M. Tensile and flexural response of 3D printed solid and porous CCFRPC structures and fracture interface study using image processing technique. J Mater Res Technol 2021;14:731–42. https://doi.org/10.1016/j.jmrt.2021.06.095.

[112] Alafaghani AA, Qattawi A, Alrawi B, Guzman A. Experimental optimization of fused deposition modelling processing parameters: a Design-for-Manufacturing approach. Procedia Manuf 2017;10:791–803. https://doi.org/10.1016/j.promfg.2017.07.079.

[113] Schneidler J, Berry C, Barari A. Improving 3D printing geometric accuracy using design of experiments on process

parameters in fused filament fabrication (FFF). In: Proceedings of 2021 14th IEEE international conference on industry applications (INDUSCON); 2021. https://doi.org/10.1109/INDUSCON51756.2021.9529615.

[114] Saenz F, Otarola C, Valladares K, Rojas J. Influence of 3D printing settings on mechanical properties of ABS at room temperature and 77 K. Addit Manuf 2021;39:101841. https://doi.org/10.1016/j.addma.2021.101841.

[115] Galetto M, Verna E, Genta G. Effect of process parameters on parts quality and process efficiency of fused deposition modeling. Comput Ind Eng 2021;156:107238. https://doi.org/10.1016/j.cie.2021.107238.

[116] Moradi M, Aminzadeh A, Rahmatabadi D, Rasouli SA. Statistical and experimental analysis of process parameters of 3D nylon printed parts by fused deposition modeling: response surface modeling and optimization. J Mater Eng Perform 2021;30:5441–54. https://doi.org/10.1007/s11665-021-05848-4.

[117] Raj MohanR, Venkatraman R, Raghuraman S. Experimental analysis on density, micro-hardness, surface roughness and processing time of acrylonitrile butadiene styrene (ABS) through fused deposition modeling (FDM) using Box behnken design (BBD). Mater Today Commun 2021;27:102353. https://doi.org/10.1016/j.mtcomm.2021.102353.

[118] Equbal A, Sood AK, Equbal MI, Badruddin IA, Khan ZA. RSM based investigation of compressive properties of FDM fabricated part. CIRP J Manuf Sci Tec 2021;35:701–14. https://doi.org/10.1016/j.cirpj.2021.08.004.

[119] Jang S, Boddorff A, Jang DJ, Lloyd J, Wagner K, Thadhani N, et al. Effect of material extrusion process parameters on filament geometry and inter-filament voids in as-fabricated high solids loaded polymer composites. Addit Manuf 2021;47:102313. https://doi.org/10.1016/j.addma.2021.102313.

[120] Heidari-Rarani M, Ezati N, Sadeghi P, Badrossamay MR. Optimization of FDM process parameters for tensile properties of polylactic acid specimens using Taguchi design of experiment method. J Thermoplast Compos 2020:1063458256. https://doi.org/10.1177/0892705720964560.

[121] Travieso-Rodriguez JA, Zandi MD, Jerez-Mesa R, Lluma-Fuentes J. Fatigue behavior of PLA-wood composite manufactured by fused filament fabrication. J Mater Res Technol 2020;9:8507–16. https://doi.org/10.1016/j.jmrt.2020.06.003.

[122] Ruberu K, Senadeera M, Rana S, Gupta S, Chung J, Yue Z, et al. Coupling machine learning with 3D bioprinting to fast track optimisation of extrusion printing. Appl Mater Today 2021;22:100914. https://doi.org/10.1016/j.apmt.2020.100914.

[123] Nasiri S, Khosravani MR. Machine learning in predicting mechanical behavior of additively manufactured parts. J Mater Res Technol 2021;14:1137–53. https://doi.org/10.1016/j.jmrt.2021.07.004.

[124] Johnson NS, Vulimiri PS, To AC, Zhang X, Brice CA, Kappes BB, et al. Invited review: machine learning for materials developments in metals additive manufacturing. Addit Manuf 2020;36:101641. https://doi.org/10.1016/j.addma.2020.101641.

[125] Sood AK, Ohdar RK, Mahapatra SS. Improving dimensional accuracy of Fused Deposition Modelling processed part using grey Taguchi method. Mater Des 2009;30:4243–52. https://doi.org/10.1016/j.matdes.2009.04.030.

[126] Li Z, Zhang Z, Shi J, Wu D. Prediction of surface roughness in extrusion-based additive manufacturing with machine learning. Robot Cim-Int Manuf 2019;57:488–95. https://doi.org/10.1016/j.rcim.2019.01.004.

[127] Meiabadi MS, Moradi M, Karamimoghadam M, Ardabili S, Bodaghi M, Shokri M, et al. Modeling the producibility of 3D printing in polylactic acid using artificial neural networks and fused filament fabrication. Polymers 2021;13:3219. https://doi.org/10.3390/polym13193219.

[128] Ö Bayraktar, Uzun G, Çakiroğlu R, Guldas A. Experimental study on the 3D-printed plastic parts and predicting the mechanical properties using artificial neural networks. Polym Adv Technol 2017;28:1044–51. https://doi.org/10.1002/pat.3960.

[129] Sood AK, Ohdar RK, Mahapatra SS. Experimental investigation and empirical modelling of FDM process for compressive strength improvement. J Adv Res 2012;3:81–90. https://doi.org/10.1016/j.jare.2011.05.001.

[130] Sood AK, Equbal A, Toppo V, Ohdar RK, Mahapatra SS. An investigation on sliding wear of FDM built parts. CIRP J Manuf Sci Tec 2012;5:48–54. https://doi.org/10.1016/j.cirpj.2011.08.003.

[131] Mohamed OA, Masood SH, Bhowmik JL. Influence of processing parameters on creep and recovery behavior of FDM manufactured part using definitive screening design and ANN. Rapid Prototyp J 2017;23:998–1010. https://doi.org/10.1108/RPJ-12-2015-0198.

[132] Mohamed OA, Masood SH, Bhowmik JL. Investigation of dynamic elastic deformation of parts processed by fused deposition modeling additive manufacturing. Adv Prod Eng Manag 2016;11:227–38. https://doi.org/10.14743/apem2016.3.223.

Peng Li is a Professor in the State Key Laboratory of Biobased Material and Green Papermaking, Qilu University of Technology (Shandong Academy of Sciences), Jinan, China. Currently, he specializes in the field of biomass composites research, design of functional products, and additive manufacturing using bio-based materials.